






Article

A Proposal for a Composite with Temperature-Independent Thermophysical Properties: HfV₂–HfV₂O₇

Philipp Keuter ^{1,*}, Anna L. Ravensburg ^{1,2}, Marcus Hans ¹, Soheil Karimi Aghda ¹,
Damian M. Holzapfel ¹, Daniel Primetzhofer ² and Jochen M. Schneider ¹

¹ Materials Chemistry, RWTH Aachen University, Kopernikusstr. 10, 52074 Aachen, Germany; anna.ravensburg@physics.uu.se (A.L.R.); hans@mch.rwth-aachen.de (M.H.); karimi@mch.rwth-aachen.de (S.K.A.); holzapfel@mch.rwth-aachen.de (D.M.H.); schneider@mch.rwth-aachen.de (J.M.S.)

² Department of Physics and Astronomy, Uppsala University, Box 516, 75120 Uppsala, Sweden; daniel.primetzhofer@physics.uu.se

* Correspondence: keuter@mch.rwth-aachen.de

Received: 9 October 2020; Accepted: 5 November 2020; Published: 7 November 2020



Abstract: The HfV₂–HfV₂O₇ composite is proposed as a material with potentially temperature-independent thermophysical properties due to the combination of anomalously increasing thermoelastic constants of HfV₂ with the negative thermal expansion of HfV₂O₇. Based on literature data, the coexistence of both a near-zero temperature coefficient of elasticity and a coefficient of thermal expansion is suggested for a composite with a phase fraction of approximately 30 vol.% HfV₂ and 70 vol.% HfV₂O₇. To produce HfV₂–HfV₂O₇ composites, two synthesis pathways were investigated: (1) annealing of sputtered HfV₂ films in air to form HfV₂O₇ oxide on the surface and (2) sputtering of HfV₂O₇/HfV₂ bilayers. The high oxygen mobility in HfV₂ is suggested to inhibit the formation of crystalline HfV₂–HfV₂O₇ composites by annealing HfV₂ in air due to oxygen-incorporation-induced amorphization of HfV₂. Reducing the formation temperature of crystalline HfV₂O₇ from 550 °C, as obtained upon annealing, to 300 °C using reactive sputtering enables the synthesis of crystalline bilayered HfV₂–HfV₂O₇.

Keywords: thermoelasticity; negative thermal expansion; composites; magnetron sputtering

1. Introduction

Volume expansion upon heating is probably the most prominent example of the influence of temperature on the physical properties of materials. However, for electronic, optical, and other high-precision devices, whose performances are critically affected by slight variations in volume, near-zero thermal expansion materials are desired [1–5]. Moreover, for mechanical components of precision instruments, temperature-independent volumes and elastic moduli are required [6–8]. A combination of both properties has only been obtained in gum metals [9,10] and Fe–Ni alloys [11] after intense deformation, thereby promoting the development of materials with intrinsic near-zero expansion and temperature-invariant elastic behavior irrespective of the plastic deformation route.

To compensate for thermally-induced volume changes, implementation of materials with negative thermal expansion (NTE) in a composite is a widely propagated approach [4,5,12]. Here, we propose to join a material with NTE properties with another exhibiting anomalously increasing thermoelastic constants in an attempt to obtain a combination of temperature-invariant elastic behavior and volume. This is a pioneering approach for the design of materials with temperature-independent thermophysical properties.

However, elastic constants commonly decrease monotonically with rising temperatures due to the anharmonicity of lattice vibrations [13,14]. Materials that deviate from this trend, thereby exhibiting anomalous thermoelastic behavior, constitute promising candidates for the design of composites with temperature-independent thermoelastic properties. While nowadays NTE has been observed in a wide variety of material families, e.g., zirconium tungstates and vanadates, zeolites, metal cyanides, metal-organic framework materials, perovskites, and anti-perovskites [12,15–18], reports of materials with anomalous thermoelastic behavior are scarce. The cubic transition metals V, Nb, Ta, Pd, and Pt each exhibit a thermoelastic anomaly in their shear elastic constants c_{44} [19–23]. Furthermore, binary Nb–Zr, Nb–Mo, Pd–Ag, and Pd–Rh solid solutions behave anomalously within well-defined concentration ranges [24–26]. Experimental and theoretical studies revealed the combination of a high density of states and electronic reallocation upon lattice distortion in the vicinity of the Fermi level to be the physical origin of the anomalous thermoelastic behavior [27–31]. However, the anomaly in these systems is mostly limited to the shear elastic constant c_{44} , whereas the remaining elastic constants (there are three independent elastic constants for cubic symmetries, i.e., c_{11} , c_{12} , and c_{44}) behave normally. Consequently, their thermoelastic anomaly is highly directionally dependent, but an isotropic temperature-independent behavior is desired for the proposed composite. Intermetallic cubic HfV₂ (space group: Fm-3m), which is stable from around 112 K up to the melting point of 1820 K [32,33], exhibits increasing thermoelastic constants in all probed directions [32] so that an increase in the macroscopic elastic modulus (E) upon heating was measured in polycrystalline samples [34,35]. Thus, HfV₂ is an ideal constituent to aim for a temperature-invariant elastic behavior in a composite. The second component, consequently, serves then for the compensation of the thermoelastic increase and for the positive thermal expansion (PTE) of HfV₂. The linear coefficient of thermal expansion of HfV₂ has been measured to be $9.9 \times 10^{-6} \text{ K}^{-1}$ around room temperature [36].

Multiple mechanisms may give rise to NTE [5,17], e.g., the magnetovolume effect, phase transitions, atomic radius contraction, and flexible network structures, whereas the latter is the prevalent physical origin in most NTE materials. In general, the expansion effect due to longitudinal vibrations in these flexible network structures is over-compensated by the contraction owing to transverse vibrations [5,37]. In regard to the search for suitable NTE materials, anisotropic contraction restricts their practical usability, so cubic phases, which exhibit inherently isotropic contraction, are particularly promising. In the group of flexible network materials, ZrW₂O₈ and isostructural HfW₂O₈ have an unprecedented isotropic NTE range of 0.3 to 1050 K [38,39]. Besides, the only ternary oxide within the Hf–V–O system, HfV₂O₇, exhibits isotropic NTE above approximately 370 K with a negative coefficient of thermal expansion of $-7.2 \times 10^{-6} \text{ K}^{-1}$ [40]. With decreasing temperature, phase transformations first into an incommensurate structure, stable between around 369 and 340 K, and finally into a cubic $3 \times 3 \times 3$ superstructure, are obtained [41]. Hence, forming a composite of HfV₂ with the corresponding ternary oxide, HfV₂O₇, appears promising for tailoring the physical properties of the composite material towards thermal invariance.

Physical vapor deposition techniques have proven to be successful in synthesizing and refining materials with NTE properties [42–45]. Consequently, after assessing that a combination of both temperature-invariant elastic behavior and volume is achieved simultaneously for a certain phase fraction ratio, two synthesis pathways for HfV₂–HfV₂O₇ composites were studied: (1) annealing of magnetron sputtered HfV₂ thin films in air to form a HfV₂O₇ oxide scale on the thin film surface and (2) magnetron sputtering of HfV₂O₇ on HfV₂. Furthermore, the NTE properties of HfV₂O₇ were verified for single-layered HfV₂O₇ thin films using temperature-dependent in situ X-ray diffraction.

2. Materials and Methods

2.1. Experimental Methods

Depositions were carried out by direct current magnetron sputtering at a target-to-substrate distance of 10 cm using elemental Hf and V (both 99.9% purity, 50 mm diameter) targets while the

substrate remained at floating potential. For the synthesis of stoichiometric HfV₂, the employed target power densities were 2.0 and 10.2 W cm⁻² for Hf and V, respectively. Ar (99.9999%) was used as sputtering gas to achieve a working pressure of 0.4 Pa. The base pressure (at deposition temperature) was below 1 × 10⁻⁶ Pa. HfV₂ films were deposited without intentional heating and at substrate temperatures of 500 and 700 °C. To ensure high purity of deposited HfV₂, the following measures were taken: The backsides of the single-crystalline sapphire (0001) substrates were deposited beforehand with approximately 250 nm of Nb to overcome their partial transmissivity to radiation during heating. This consequently reduced the heat impact on the chamber walls, and thus, a considerable decrease in base pressure at elevated deposition temperatures was achieved. Second, prior to each deposition, all targets were sputtered for 5 min with closed shutters (positioned approximately 2 cm opposite of the target) to make the surfaces free from condensed impurities and to getter residual gases. Third, elemental Zr was additionally sputtered at 20 W against a shutter during all depositions to exploit its pronounced affinity for oxygen [46,47] as a getter pump to further reduce residual gas incorporation [48] into the growing HfV₂ thin film. The Zr concentration in the as-deposited films was below 0.7 at.% based on energy-dispersive X-ray spectroscopy (EDX). Subsequently, selected films were capped after cooling to room temperature with an approximately 10 nm thick Nb layer to prevent impurity incorporation into the as-deposited thin film during air exposure.

HfV₂O₇ thin films were deposited at a substrate temperature of 450 °C in a reactive Ar/O₂ (99.999%) atmosphere at a constant working pressure of 0.86 Pa while varying the O₂ partial pressure between 0.05 and 0.13 Pa. Further information can be found elsewhere [49]. For the HfV₂-HfV₂O₇ bilayer deposition, the synthesis procedure was the following: First, HfV₂ was deposited at 700 °C for 75 min. Afterwards, the system was cooled down in vacuum to the synthesis substrate temperatures for HfV₂O₇, which were 250, 300, and 350 °C. Pure Ar was used for plasma ignition before O₂ (p_{O2} = 0.09 Pa) was introduced to reactively sputter HfV₂O₇ for 100 min.

Annealing experiments were performed in a GERO F 40-200/13 air furnace (Carbolite Gero, Neuhausen, Germany). The Hf-V ratio in the synthesized films was measured by EDX carried out in a JEOL JFM-6480 SEM (JEOL Ltd., Tokyo, Japan) equipped with an EDAX Genesis 2000 device (EDAX Inc., Mahwah, NJ, USA) at an acceleration voltage of 20 kV. Chemical composition depth profiling of HfV₂ was done by time-of-flight elastic recoil detection analysis (ToF-ERDA) at the Tandem Accelerator Laboratory of Uppsala University. 36 MeV ¹²⁷I⁸⁺ primary ions and a time-of-flight telescope in combination with a Si solid-state detector for energy discrimination were used. Further details on the detector telescope can be found elsewhere [50]. The time and energy coincidence spectra were evaluated using the CONTES software package [51]. O and H depth profiles were characterized by ToF-ERDA, while the Hf-V ratio was obtained from EDX spectra. It should be noticed that Nb-capped and uncapped HfV₂ were measured by ToF-ERDA under identical conditions, hence, systematic uncertainties do not affect this comparison. The structure of the synthesized films was studied using X-ray diffraction (XRD) carried out with a Bruker AXS D8 Discover General Area Detector Diffraction System (Bruker Corporation, Billerica, MA, USA). A Cu K_α source (current 40 mA, voltage of 40 kV) was used with a 0.5 mm pinhole collimator. Scans were performed at a fixed incidence angle of 15°. Selected samples were measured between room temperature and 475 °C using a DHS 1100 Hot Stage (Anton Paar, Ostfildern-Schornhausen, Germany) equipped with a Ni-NiCr thermocouple to measure the surface temperature. Peak fitting was conducted using TOPAS software (version 3) with a pseudo-Voigt II function. Lattice parameters of the cubic structures were consequently calculated employing Bragg's law [52]. The lattice parameters of HfV₂ were determined by averaging the data from (220), (311), (222), (331), (422), (333), and (044) reflections. Based on the obtained changes in lattice parameters with temperature, the linear coefficient of thermal expansion for cubic HfV₂O₇ was calculated by averaging the data from (200), (210), (211), (211), (220), (311), and (222) reflections. Standard deviations are added to evaluate the fitting quality. Morphology of bilayered HfV₂-HfV₂O₇ was studied using scanning transmission electron microscopy (STEM) carried out in an FEI Helios Nanolab 660 dual-beam microscope (Thermo Fisher Scientific, Waltham, MA, USA). Cross-sectional

sample preparation was conducted by focused ion beam techniques with a Ga⁺ source following a standard lift-out procedure [53].

2.2. Theoretical Methods

Ground state equilibrium lattice parameters for cubic HfO₂ (Fm-3m, 12 atoms), VO₂ (Fm-3m, 12 atoms), VO (Fm-3m, 8 atoms), and HfO (Fm-3m, 8 atoms) were calculated within the framework of density functional theory (DFT) [54] employing the Vienna ab initio simulation package (VASP) [55,56] with projector augmented wave potentials. The generalized gradient approximation, as introduced by Perdew, Burke, and Ernzerhof [57], was used for all calculations. Integration in the Brillouin zone was performed on a 20 × 20 × 20 *k*-point grid according to Monkhorst and Pack [58]. The total energy convergence criterion was 0.01 meV within a 500 eV cut-off. The equilibrium lattice parameters were determined by a Birch–Murnaghan equation of state [59,60] fit.

3. Results and Discussion

3.1. Composite Assessment

First, the suitability of HfV₂–HfV₂O₇ as a composite with temperature-independent physical properties is evaluated, which relies on the coexistence of a near-zero coefficient of thermal expansion and a near-zero temperature coefficient of elasticity (TCE) for a certain phase fraction ratio. The TCE is defined by

$$TCE = \frac{1}{E} \frac{dE}{dT} \quad (1)$$

and is estimated for HfV₂–HfV₂O₇ composite using a rule-of-mixture approach (weighted average based on the volume fractions). While the temperature dependence of the elastic modulus of HfV₂ is taken from the literature [35], no thermoelasticity data for HfV₂O₇ have been reported. The temperature-dependent elastic modulus has consequently been estimated from the experimentally obtained elastic modulus of HfV₂O₇ [49] assuming the same relative decline with temperature, as reported for the NTE material ZrW₂O₈ [61]. ZrW₂O₈ and HfV₂O₇ exhibit comparable negative coefficients of thermal expansion of -9.1×10^{-6} [62] and $-7.2 \times 10^{-6} \text{ K}^{-1}$ [40], respectively, and share common structural features, both forming an openly-packed network structure of octahedral (Zr/Hf)O₆ and polyhedral (W/V)O₄ units connected by corner-sharing oxygen atoms [63]. The TCE of the composite was averaged over a temperature range from 120 (onset of NTE behavior in HfV₂O₇ [40,41,64]) to 300 °C.

On the other hand, the coefficient of thermal expansion of a composite usually does not follow a simple rule-of-mixture behavior [65]. NTE materials are generally less stiff (lower *E*) than expected based on the bond strengths [66], and thus normally constitute the more compliant component in the composite. As a result, the elastic deformation during expansion and contraction is predominantly concentrated on the NTE component reducing its impact on the overall expansion coefficient. Consequently, theoretical models to describe the expansion coefficient of a composite typically also take the elastic properties of the individual components into account [66]. In the Turner model the overall coefficient of thermal expansion of the composite α_c is described by

$$\alpha_c = \frac{\sum_i B_i \alpha_i \phi_i}{\sum_i B_i \phi_i}, \quad (2)$$

where B_i , α_i , and ϕ_i denote the bulk modulus, coefficient of thermal expansion, and volume fraction, respectively, of component *i* [65]. The bulk modulus and the coefficient of thermal expansion of HfV₂ (HfV₂O₇) of 117 GPa [32] (56 GPa [49]) and $9.9 \times 10^{-6} \text{ K}^{-1}$ [36] ($-7.2 \times 10^{-6} \text{ K}^{-1}$ [40]), respectively, were used for the calculation of α_c . The resulting volume fraction dependent expansion coefficient α_c and averaged TCE of HfV₂–HfV₂O₇ composite are plotted in Figure 1.

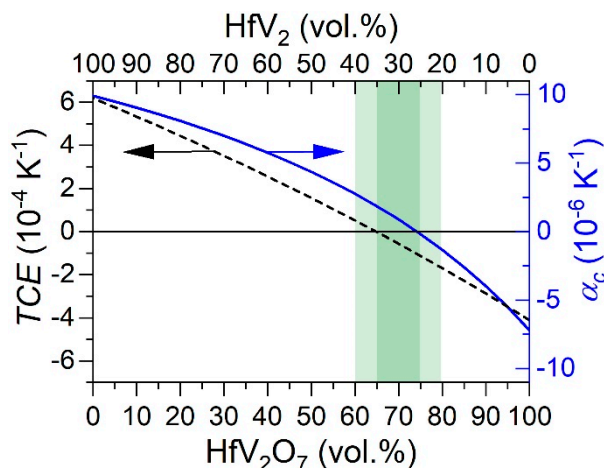


Figure 1. Variation of the temperature coefficient of elasticity TCE (black dashed line) and linear coefficient of thermal expansion α_c (blue solid line) of composite material HfV_2 – HfV_2O_7 depending on the volume fractions of the individual constituents. The region of interest is highlighted in green.

The coefficient of thermal expansion of the composite was calculated to reach temperature invariance ($\alpha_c = 0$) at a volume fraction of HfV_2 of around 0.25 ($\phi_{HfV_2O_7} = 0.75$). A TCE of zero was achieved for ϕ_{HfV_2} of around 0.35 ($\phi_{HfV_2O_7} = 0.65$) with a corresponding α_c of $1.9 \times 10^{-6} K^{-1}$, which complies with the class of very low thermal expansion materials [1]. These results not only suggest that α_c and TCE of this composite can individually be adjusted to thermal invariance but also that a near-zero α_c and TCE may be achieved simultaneously. Based on the applied data and the assumptions outlined above, we predict that the corresponding volume phase fractions of HfV_2 (HfV_2O_7) are between 20 and 40 (80–60) vol.% depending on the optimization criterion. After assessing the capability of composite HfV_2 – HfV_2O_7 to exhibit temperature-independent properties, its synthesis is studied in the following.

3.2. Composite Formation by Oxidation of HfV_2

A potential synthesis pathway for a composite has been demonstrated by oxidizing TiN thin films, where the time- and temperature-dependent formation of a TiO_2 scale on top of TiN was observed with varying thickness, and hence phase fraction ratios [67,68]. Consequently, the first synthesis strategy to form HfV_2 – HfV_2O_7 composites comprises synthesis of HfV_2 and subsequent heat treatment in air to partly oxidize HfV_2 in an attempt to form a HfV_2O_7 oxide scale on top.

3.2.1. Phase Formation of HfV_2

First, the phase formation for co-sputtered Hf-V thin films using magnetron sputtering is described. No previous reports on the synthesis of HfV_2 thin films by magnetron sputtering are currently available. However, the synthesis of isoelectronic and isostructural ZrV_2 thin films is discussed in the literature [69–71]. EDX analysis of the as-deposited thin films shows deviations from the desired 1Hf:2V stoichiometry below ± 1 at.%. The results of the structural analysis to study the influence of the deposition temperature on the phase formation are depicted in Figure 2.

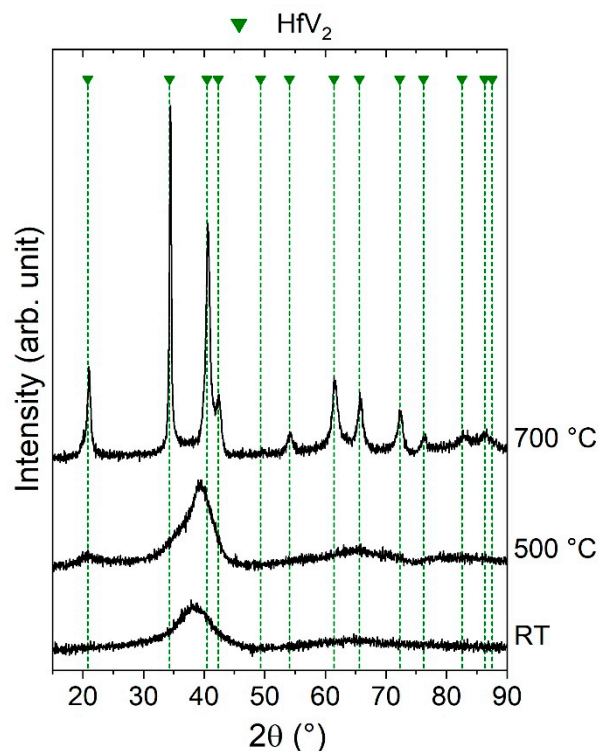


Figure 2. X-ray diffractograms of stoichiometric (V/Hf = 2.0) Hf-V samples synthesized without intentional heating (RT) and at synthesis temperatures of 500 and 700 °C.

A broad hump around 40° was obtained for HfV₂ deposited without intentional heating (RT), indicating an amorphous structure, as reported for magnetron sputtered Zr–V thin films deposited without heating [71] and at 400 °C [70]. In this temperature regime, in which the adatom mobility is low, the formation of amorphous solid solution in Zr–V can be understood based on its higher stability compared to a random bcc solid solution, as demonstrated by DFT calculations [71]. It is reasonable to assume that this may also apply to Hf–V.

For Zr–V, a phase formation sequence from amorphous (400 °C) to a phase mixture of bcc V and hcp Zr (500 °C) to intermetallic ZrV₂ (600 °C) was obtained with increasing deposition temperatures [70]. The same sequence was obtained by annealing amorphous films [70]. The intermediate formation of bcc V and hcp Zr is contradictory to the accepted equilibrium phase diagram and is mostly discussed with respect to difficult nucleation kinetics of the Laves phase structure [69,70]. However, it may also be explained by the thermodynamic instability of cubic ZrV₂, as predicted by DFT in the ground state [71–73], exhibiting an energy of formation of 150 meV atom^{−1} [71], which persists at elevated temperatures. In comparison, several theoretical studies also predict cubic HfV₂ to be energetically unstable in the ground state, reporting energies of formation between 20 and 35 meV per atom [29,74,75]. Furthermore, experiments show a transformation of cubic HfV₂ upon cooling into an orthorhombic structure at around −160 °C [76,77] possibly due to kinetically limited decomposition into elemental V and Hf, since orthorhombic HfV₂ also exhibits positive energy of formation [29,75]. However, for sputtered HfV₂ at 500 °C (see Figure 2), the change in shape of the main peak at around 38° suggests the first formation of nanocrystals, and the emerging hump around 20° points towards intermetallic HfV₂ nanocrystals, since their presence cannot be explained by hcp Hf or bcc V.

A further increase in deposition temperature to 700 °C resulted in the formation of sharp diffraction peaks which all can be assigned to cubic HfV₂ [78]. Thus, no phase mixture of hcp Hf and bcc V, unlike for Zr–V, was observed, but a sequence from amorphous to crystalline HfV₂ with increasing deposition temperature was obtained. Consequently, the high temperature of 700 °C required to form crystalline HfV₂ is attributed to the kinetically limited formation of the Laves phase structure and not

to an energetic instability of the cubic structure up to these temperatures. This notion is supported by theoretical predictions suggesting the energetic stabilization of cubic HfV_2 at temperatures as low as -120°C due to lattice vibrations [29]. For ZrV_2 , due to the considerably higher energy of formation in the ground state [71], its energetic stabilization is expected at higher temperatures, potentially explaining the discussed phase formation differences between Hf-V and Zr-V thin films. For comparison, bulk synthesis of HfV_2 includes heat treatments at temperatures above 1200°C [34,77,79]. The reduction in synthesis temperature to 700°C is enabled by surface diffusion of adatoms during sputtering [80].

No indications for impurity phases based on the presented XRD results were obtained in these samples, which is ascribed to the measures outlined above. However, thin films synthesized at higher base pressures or without additional co-sputtering of Zr contained traces of $\text{Hf}_3\text{V}_3\text{O}$ and HfO_2 (not shown). This is in agreement with the observation of ZrV_3O_3 as an impurity phase in sputtered Zr-V thin films [70].

3.2.2. Stability of HfV_2

As a next step, the stability of the synthesized HfV_2 films upon air exposure is examined. For this purpose, the structure of uncapped HfV_2 was studied as a function of the cumulated air-exposure time after removing it from the high-vacuum deposition system. The results are summarized in Figure 3.

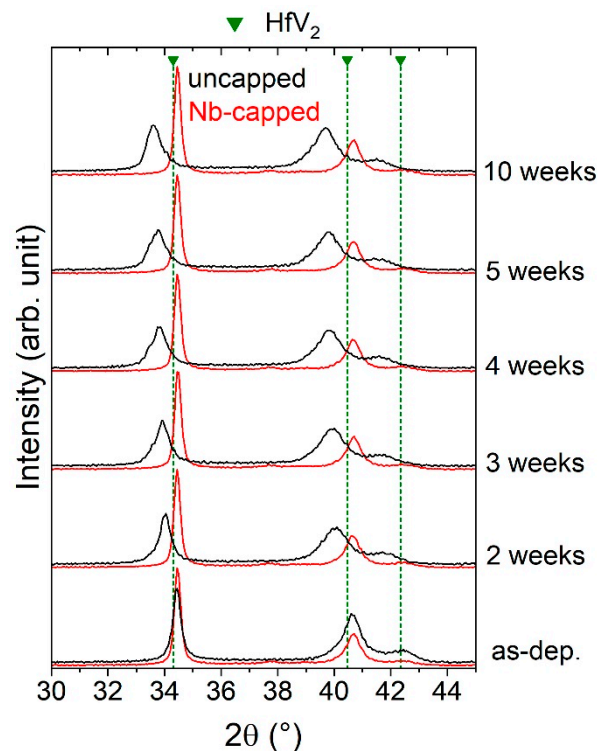


Figure 3. X-ray diffractograms of uncapped HfV_2 (black) and Nb-capped HfV_2 (red) for varying storage times in air.

In the as-deposited state, referring to a minimized air-exposure time of approximately 15 min, the peak positions coincide well with literature data for cubic HfV_2 [78]. With increasing air-exposure time, a continuous peak shift to lower 2θ values is obtained, indicating an increase in the lattice parameter of the cubic structure from 7.38 to 7.51 Å (+1.8%) after four and to 7.54 Å (+2.2%) after ten weeks in air (standard deviations ≤ 0.01 Å). The obtained increase in lattice parameter may suggest continuous interstitial incorporation of impurities into the HfV_2 lattice, which consequently also explains reported property changes in (Hf,Zr) V_2 bulk samples after a one-year storage period [81]. HfV_2 has been reported to act as a strong (weak) getter for hydrogen (oxygen) by dissociation of water [82].

Thin metal capping layers were shown to serve as effective oxidation barriers during air exposure at room temperature [83]. Hence, as-deposited HfV₂ was capped with approximately 10 nm Nb due to its passivating properties [84]. The functionality of this capping layer was investigated systematically by comparing the stabilities of capped and uncapped HfV₂ using XRD (see Figure 3). Other than a small additional peak around 38°, measured for the Nb-capped film, which is attributed to bcc Nb, no difference in phase composition between both HfV₂ films in the as-deposited state was observed. However, in contrast to the uncapped HfV₂ film, no peak shift with increasing air-exposure time was obtained, demonstrating that the Nb capping ensures protection of synthesized HfV₂ against the incorporation of impurities from the ambient at room temperature.

To identify the incorporated impurities, the chemical compositions of both samples, uncapped and Nb-capped, were analyzed four weeks after deposition using ToF-ERDA. The measured oxygen concentration as a function of the film thicknesses is presented in Figure 4. The depth scale was calculated with the atomic masses of Hf and V under the assumption of stoichiometric HfV₂ with a density of 9.3 g cm⁻³ [32].

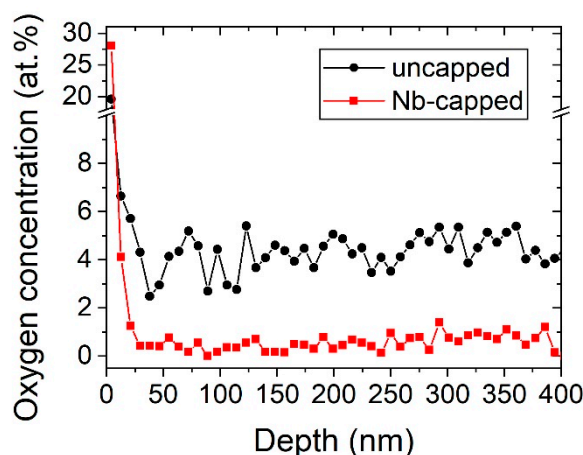


Figure 4. ToF-ERDA depth profile of the oxygen concentration for uncapped (black circle) and Nb-capped (red square) HfV₂ after four weeks of air-exposure.

Uncapped HfV₂ exhibited an averaged oxygen concentration of 4.3 ± 0.7 at.% in the bulk part of the film (neglecting the top surface oxidation) and a minor amount of hydrogen (<0.3 at.%, not shown) while the average oxygen concentration in the Nb-capped film was 0.5 ± 0.3 at.% and hydrogen was below the detection limit. Thus, the increasing lattice parameter for uncapped HfV₂ is primarily attributed to a continuous interstitial uptake of oxygen into the cubic structure upon exposure to air. It has been shown theoretically that interstitially incorporated oxygen contributes to the energetic and mechanical stabilization of the cubic structure [29]. The oxygen concentration was measured to be constant throughout the analyzed film thickness of approximately 400 nm, suggesting high mobility of oxygen in cubic HfV₂ already at room temperature. This may also have implications for the oxidation behavior of these films at elevated temperatures, which is discussed in the following.

3.2.3. Oxidation of HfV₂

One sample of uncapped HfV₂ was cyclically annealed in air for approximately 30 min at temperatures between 150 and 650 °C in 100 °C intervals. After each annealing step, the structure of the sample was studied by XRD. The resulting diffractograms are shown in Figure 5.

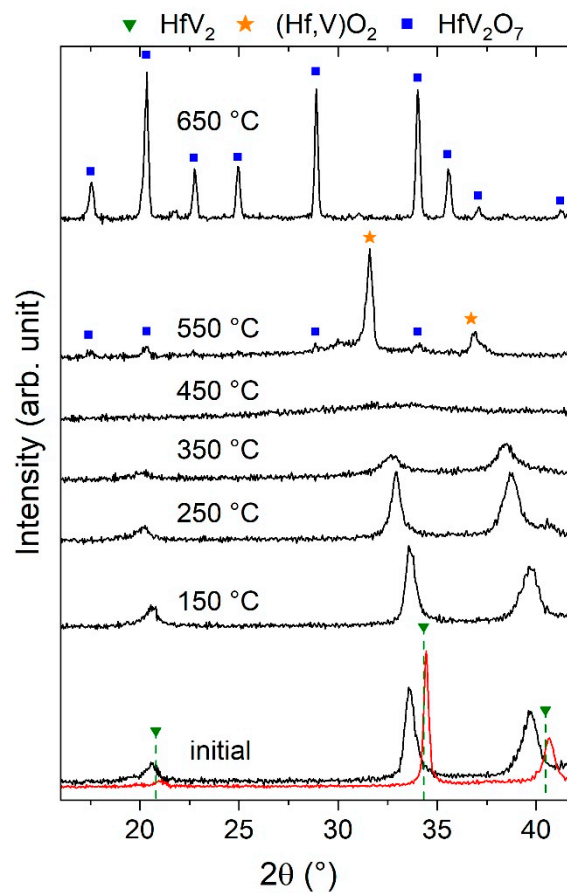


Figure 5. X-ray diffractograms of an uncapped HfV_2 thin film (9 weeks after deposition) annealed at the indicated temperatures for approximately 30 min. For comparison, the diffractogram of a Nb-capped film was added (red).

In the initial state, the sample was already exposed to air for 9 weeks. As a consequence, peak positions were already shifted towards smaller 2θ values compared to the as-deposited (see Figure 3) and Nb-capped films (see Figure 5). For all annealing steps up to 350 °C, the structural development is characterized by a continuous peak shift and broadening suggesting the successive incorporation of oxygen into the cubic structure finally yielding amorphization, as observed at 450 °C. Complementary annealing experiments with additional samples at fixed temperatures of 300 and 400 °C indicate that this process is determined by kinetics and may occur already at lower temperatures (not shown).

After annealing at 550 °C, small peaks emerged which may already indicate the formation of HfV_2O_7 nanocrystals [41], while the two main peaks at 32° and 37° cannot be attributed to any reported equilibrium phase in the Hf-V-O materials system. The peak positions of the unknown phase fit reasonably well to a cubic (fcc-based) structure exhibiting a lattice parameter of 4.9 Å. The reported cubic structures in the Hf-V-O systems, VO ($\text{Fm}\bar{3}\text{m}$) [85] and HfO_2 ($\text{Fm}\bar{3}\text{m}$) [86], can be excluded due to the difference in the lattice parameters. Furthermore, the formation of a hypothetical cubic $\text{Hf}_{1-x}\text{V}_x\text{O}$ monoxide appears unlikely based on conducted DFT studies, predicting a lattice parameter between 4.19 and 4.58 Å for $x = 0$ and $x = 1$, respectively. Nevertheless, the experimentally obtained lattice parameter lies within the predicted lattice parameter range of a previously unreported $\text{Hf}_{1-x}\text{V}_x\text{O}_2$ dioxide ($\text{Fm}\bar{3}\text{m}$) which is between 5.08 and 4.74 Å for $x = 0$ and $x = 1$, respectively. Hence, the formation of a metastable ternary $(\text{Hf},\text{V})\text{O}_2$ phase is assumed henceforth. A high V solubility in cubic HfO_2 has also been reported elsewhere [87]. At 650 °C, the formation of XRD phase pure HfV_2O_7 is evident [41].

The observation that the first crystallites of HfV_2O_7 may form at temperatures of 550 °C while oxygen is highly mobile in HfV_2 already at room temperature suggests that the formation of HfV_2 - HfV_2O_7 composites is not feasible using conventional annealing experiments in air. The oxygen

mobility in HfV_2 at the formation temperature of crystalline HfV_2O_7 appears to be critical for the endeavor of HfV_2 – HfV_2O_7 composite formation. However, lowering of the synthesis temperature of crystalline HfV_2O_7 by using non-equilibrium-based synthesis approaches appears promising and is discussed in the following.

3.3. Composite Formation by Sputtering of Bilayered HfV_2 – HfV_2O_7

3.3.1. Phase Formation of HfV_2O_7

The formation of crystalline HfV_2O_7 at a substrate temperature of 350 °C using reactive magnetron sputtering has been demonstrated previously [49], but the effect of the O_2 partial pressure has not been investigated yet. However, for the synthesis of bilayered HfV_2 – HfV_2O_7 by magnetron sputtering, the O_2 partial pressure during the synthesis of HfV_2O_7 is expected to be decisive for the purity of the underlying HfV_2 film, due to its high oxygen affinity. Hence, the influence of the O_2 partial pressure on the phase formation of HfV_2O_7 was studied systematically for a synthesis temperature of 450 °C. The results of the structural analysis of synthesized thin films, exhibiting a V–Hf ratio of 2.0 based on EDX, are shown in Figure 6.

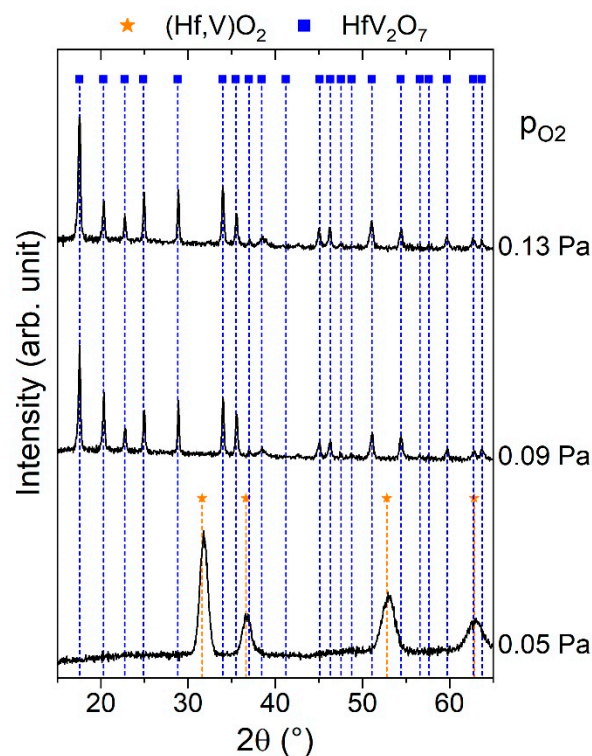


Figure 6. X-ray diffractograms of reactively sputtered Hf–V–O (V/Hf = 2) thin films deposited at 450 °C with varying O_2 partial pressure.

The thin film sputtered at an O_2 partial pressure of 0.05 Pa exhibits broad peaks at around 32°, 37°, 53°, and 63°. The peak positions coincide well with the ones of the cubic $(\text{Hf},\text{V})\text{O}_2$ structure observed during annealing of HfV_2 at 550 °C (see Figure 5). Cubic HfO_2 usually constitutes the high-temperature polymorph, which is stable above 2600 °C at ambient pressure [86] but can be stabilized down to room temperature by V doping in specific atmospheres (oxidation state $\leq \text{V}^{4+}$) [88]. Furthermore, cubic HfO_2 thin films form by ion beam assisted deposition under oxygen deficiency and substrate cooling [89]. Thus, it is assumed that the formation of cubic $(\text{Hf},\text{V})\text{O}_2$ obtained for the lowest O_2 partial pressure is triggered by oxygen deficiency. This notion is supported by the fact that the increase in the O_2 partial pressure from 0.05 to 0.09 Pa resulted in a sixfold decrease in deposition rate (with respect to the mass gain), which indicates a more pronounced poisoning of the target racetrack. For O_2 partial pressures

of 0.09 and 0.13 Pa, all obtained peaks can be assigned to the HfV_2O_7 structure [41], indicating the formation of phase pure HfV_2O_7 based on XRD.

3.3.2. Thermal Expansion of Sputtered HfV_2O_7

While numerous NTE materials have intensively been studied in bulk, studies on thin films are scarce [42–45]. To verify the NTE behavior of the synthesized HfV_2O_7 thin films, temperature-dependent in situ XRD measurements were performed to measure the change in the lattice parameter upon heating. The results are shown in Figure 7.

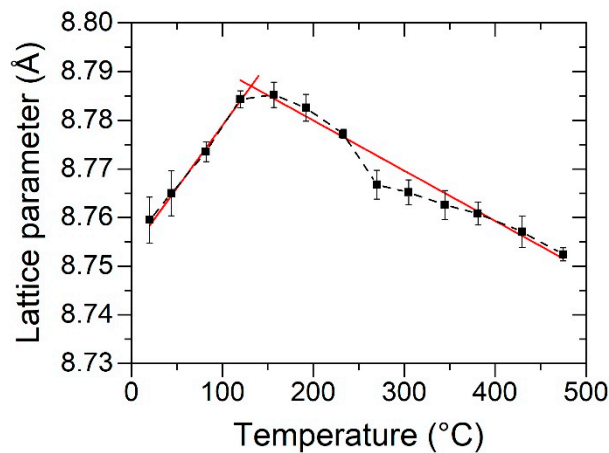


Figure 7. Lattice parameter of synthesized cubic HfV_2O_7 as a function of annealing temperature obtained by X-ray diffraction. A linear fit within the positive and negative thermal expansion range, respectively, was added (red).

A continuous increase in the lattice parameter between 20 and 120 °C was measured, whereas between 155 and 475 °C the lattice parameter decreased, indicating NTE. The obtained transition from PTE to NTE is in agreement with reported transition temperatures of HfV_2O_7 being around 120–130 °C produced by solid-state reaction synthesis approaches [40,41,64]. Additional wafer curvature measurements confirm this transition, as indicated by a change from increasing compressive to increasing tensile stress upon heating (not shown). The NTE properties of HfV_2O_7 originate from its openly-packed network structure consisting of octahedral HfO_6 and tetrahedral VO_4 units, constituting quasi-rigid building blocks that are interconnected by corner-sharing oxygen atoms [4,90,91]. Three of four oxygen atoms of the VO_4 tetrahedron are shared with neighboring HfO_6 octahedra, while one is shared with another VO_4 tetrahedron, thereby forming a V_2O_7 group [92]. The lattice symmetry (space group: $\text{Pa}\bar{3}$) restricts these $\text{O}_3\text{V}-\text{O}-\text{VO}_3$ bonds to retain an angle of 180°, allowing for transverse vibrations that may give rise to NTE [4,93]. The loss of the NTE properties at lower temperatures is related to structural transitions. HfV_2O_7 transforms upon cooling via an intermediate incommensurate structure to a $3 \times 3 \times 3$ superstructure [41,64]. It has been shown for isostructural ZrV_2O_7 that the majority of the $\text{O}_3\text{V}-\text{O}-\text{VO}_3$ linkages bend away from 180° in the $3 \times 3 \times 3$ superstructure [94–96]. However, the additional weak reflections of the HfV_2O_7 superstructure [97] could not be resolved by XRD in this work. Based on the presented data, the linear coefficients of thermal expansion were determined to be $(2.8 \pm 0.5) \times 10^{-5} \text{ K}^{-1}$ ($20 \text{ °C} \leq T \leq 120 \text{ °C}$) and $(-9.9 \pm 0.9) \times 10^{-6} \text{ K}^{-1}$ ($155 \text{ °C} \leq T \leq 475 \text{ °C}$), respectively, agreeing reasonably well with the reported linear coefficients of thermal expansion of $2.5 \times 10^{-5} \text{ K}^{-1}$ [64] and $-7.2 \times 10^{-6} \text{ K}^{-1}$ [40]. After establishing a synthesis recipe for NTE material HfV_2O_7 that is characterized by a low required O_2 partial pressure, the way is paved for the synthesis of bilayered $\text{HfV}_2-\text{HfV}_2\text{O}_7$ composites using a two-staged sputtering process.

3.3.3. Phase Formation of HfV₂–HfV₂O₇ Bilayers

Besides a low O₂ partial pressure during reactive sputtering of HfV₂O₇, the synthesis temperature for HfV₂O₇ is decisive for avoiding substantial oxygen incorporation into HfV₂. Hence, the influence of synthesis temperature of HfV₂O₇, which was varied between 250 and 350 °C, on the phase formation of HfV₂–HfV₂O₇ composite was investigated by maintaining a low O₂ partial pressure of 0.09 Pa (see Figure 6). While a Nb passivation layer ensures protection of HfV₂ in air at room temperature (see Figure 3), additional bilayer depositions revealed that the deposition of a Nb interlayer, separating the two layers in the composite, does not prevent oxygen incorporation in HfV₂ during reactive sputtering of HfV₂O₇ (not shown) and is therefore not discussed further. The results of the structural analysis are shown in Figure 8.

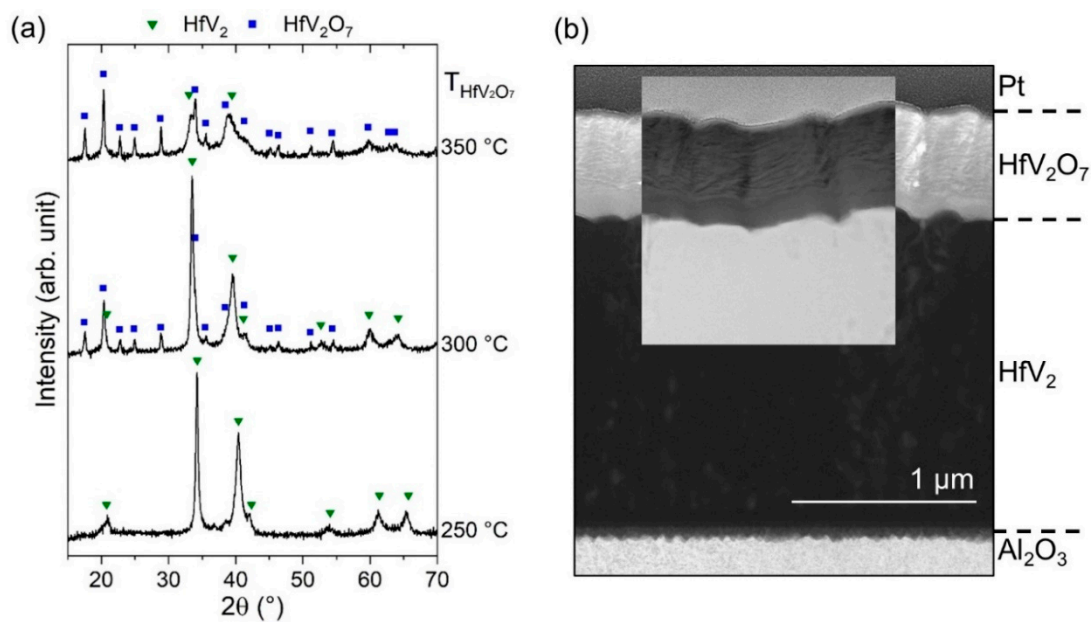


Figure 8. (a) Diffractograms of magnetron sputtered HfV₂–HfV₂O₇ bilayers. The synthesis temperature T for HfV₂O₇ on HfV₂ has been varied between 250 and 350 °C. (b) Scanning transmission electron microscopy bright-field with inset high-angle annular dark-field image of HfV₂–HfV₂O₇ cross-section with HfV₂O₇ having been synthesized at 300 °C.

For a synthesis temperature of 250 °C, peaks that are attributed to HfV₂ are barely shifted [78] indicating a low concentration of interstitially incorporated oxygen into the structure during the reactive sputtering process of HfV₂O₇. However, no distinct HfV₂O₇ peaks were obtained indicating an amorphous or nanocrystalline structure. It is expected that amorphous HfV₂O₇ does not exhibit NTE. While crystalline ZrW₂O₈ exhibits NTE in its entire stability range [38,39], PTE was obtained for amorphous ZrW₂O₈ films synthesized by reactive sputtering [42].

An increase in synthesis temperature to 300 °C results in more pronounced oxygen incorporation in HfV₂, as indicated by the increasing peak shift, which corresponds to the shift obtained for a 10-weeks exposure time of uncapped HfV₂ to air (see Figure 3). Besides, peaks of crystalline HfV₂O₇ emerge, demonstrating the first synthesis of a crystalline HfV₂–HfV₂O₇ composite. The effect of minute concentrations of interstitially solved oxygen on the thermoelastic anomaly of HfV₂ has not been studied yet and is hence proposed for future investigations. Figure 8b shows the corresponding film cross-section studied by STEM. The image suggests the formation of a bilayered structure with a defined interface separating the HfV₂ bottom layer (1.7 μm) from HfV₂O₇ (0.5 μm) top layer. Based on the atomic number (z) contrast using high-angle annular dark-field imaging, the distinct formation of HfV₂ (high z) and HfV₂O₇ (low z) is supported. The deposition rates for HfV₂ and HfV₂O₇ were determined to be approximately 22 and 5 nm min^{−1}, respectively. Thus, tuning the volume phase fractions to be in

line with the proposed ones (see Figure 1) can simply be achieved by adjusting the deposition times for the individual layer. However, further investigations are required to evaluate whether these bilayered composite films allow for accurate determination of their integral temperature coefficient of elasticity and coefficient of thermal expansion. A further increase in the synthesis temperature of HfV_2O_7 to $350\text{ }^\circ\text{C}$ reveals the onset of amorphization of HfV_2 due to oxygen incorporation, as indicated by the pronounced peak shifting and broadening.

4. Conclusions

The $\text{HfV}_2\text{--HfV}_2\text{O}_7$ composite has been proposed as a material with temperature-independent thermophysical properties due to the combination of the anomalously increasing thermoelastic constants of HfV_2 and the negative thermal expansion of HfV_2O_7 . Both the temperature coefficient of elasticity and the coefficient of thermal expansion were predicted to be near zero for a phase fraction of approximately 30 vol.% HfV_2 and 70 vol.% HfV_2O_7 .

Two synthesis pathways for $\text{HfV}_2\text{--HfV}_2\text{O}_7$ composites were studied: (1) annealing of magnetron sputtered HfV_2 thin films in air to form a HfV_2O_7 oxide scale on the thin film surface and (2) magnetron sputtering of $\text{HfV}_2\text{O}_7/\text{HfV}_2$ bilayers. The onset of the oxidation behavior of HfV_2 thin films is characterized by continuous interstitial incorporation of oxygen, occurring already at room temperature, finally yielding amorphization. Crystalline HfV_2O_7 forms at $550\text{ }^\circ\text{C}$. The high oxygen mobility in HfV_2 is suggested to inhibit the formation of crystalline $\text{HfV}_2\text{--HfV}_2\text{O}_7$ composites by annealing HfV_2 in air. Reducing the formation temperature of crystalline HfV_2O_7 down to $300\text{ }^\circ\text{C}$ using reactive magnetron sputtering enables the synthesis of a crystalline bilayered $\text{HfV}_2\text{--HfV}_2\text{O}_7$ composite. The NTE properties of HfV_2O_7 were verified for monolithic magnetron sputtered HfV_2O_7 thin films using temperature-dependent in situ X-ray diffraction.

Author Contributions: P.K., A.L.R., and J.M.S. conceived and designed the experiments and DFT calculations. A.L.R. and P.K. performed the sputtering experiments, the EDX and XRD analyses, and the DFT calculations. D.M.H. supported A.L.R. with the temperature-dependent in situ XRD measurements. ERDA measurements and data analysis were conducted by M.H. and D.P. STEM was performed by M.H. and S.K.A. All authors contributed to the evaluation and interpretation of the experimental and theoretical results. The manuscript was primarily written by P.K. with input from all authors. All authors have read and agreed to the published version of the manuscript.

Funding: Simulations were performed with computing resources granted by JARA-HPC from RWTH Aachen University under project JARA0131. Support for the operation of the accelerator laboratory in Uppsala by VR-RFI (contract 2017-00646-9) and the Swedish Foundation for Strategic Research (SSF, contract RIF14-0053) is gratefully acknowledged. The authors also kindly acknowledge funding through the Max Planck Fellow Program.

Conflicts of Interest: The authors declare no conflict of interest.

References

1. Roy, R.; Agrawal, D.K.; McKinstry, H.A. Very low thermal expansion coefficient materials. *Annu. Rev. Mater. Sci.* **1989**, *19*, 59–81. [[CrossRef](#)]
2. Wolff, E.G. Thermal expansion in metal/lithia-alumina-silica (LAS) composites. *Int. J. Thermophys.* **1988**, *9*, 221–232. [[CrossRef](#)]
3. Mandal, S.; Chakrabarti, S.; Das, S.K.; Ghatak, S. Synthesis of low expansion ceramics in lithia–alumina–silica system with zirconia additive using the powder precursor in the form of hydroxyhydrogel. *Ceram. Int.* **2007**, *33*, 123–132. [[CrossRef](#)]
4. Lind, C. Two decades of negative thermal expansion research: Where do we stand? *Materials* **2012**, *5*, 1125–1154. [[CrossRef](#)]
5. Takenaka, K. Negative thermal expansion materials: Technological key for control of thermal expansion. *Sci. Technol. Adv. Mater.* **2012**, *13*, 013001. [[CrossRef](#)]
6. Feng Huang, L.; Zeng, Z. Lattice dynamics and disorder-induced contraction in functionalized graphene. *J. Appl. Phys.* **2013**, *113*, 083524. [[CrossRef](#)]

7. Saito, T.; Furuta, T.; Hwang, J.-H.; Kuramoto, S.; Nishino, K.; Suzuki, N.; Chen, R.; Yamada, A.; Ito, K.; Seno, Y.; et al. Multifunctional alloys obtained via a dislocation-free plastic deformation mechanism. *Science* **2003**, *300*, 464–467. [[CrossRef](#)]
8. Cahn, R.W. An unusual Nobel Prize. *Notes Rec. R. Soc.* **2005**, *59*, 145–153. [[CrossRef](#)]
9. Wang, Y.; Gao, J.; Wu, H.; Yang, S.; Ding, X.; Wang, D.; Ren, X.; Wang, Y.; Song, X.; Gao, J. Strain glass transition in a multifunctional β -type Ti alloy. *Sci. Rep.* **2014**, *4*, 3995. [[CrossRef](#)]
10. Oh, J.M.; Kang, J.-H.; Lee, S.; Kim, S.-D.; Kang, N.; Park, C.H. Origin of superproperties of Ti-23Nb-1Ta-2Hf-O alloy. *Mater. Lett.* **2018**, *233*, 162–165. [[CrossRef](#)]
11. Qin, F.; Lu, F.; Chen, Y.; Yang, J.; Zhao, X. Deformation induced elinvar behavior in Fe–Ni invar alloy. *Sci. Bull.* **2018**, *63*, 1040–1042. [[CrossRef](#)]
12. Dove, M.T.; Fang, H. Negative thermal expansion and associated anomalous physical properties: Review of the lattice dynamics theoretical foundation. *Rep. Prog. Phys.* **2016**, *79*, 066503. [[CrossRef](#)] [[PubMed](#)]
13. Grimvall, G. *Thermophysical Properties of Materials*; Elsevier Science B.V.: Amsterdam, The Netherlands, 1999. [[CrossRef](#)]
14. Wachtman, J.B.; Tefft, W.E.; Lam, D.G.; Apstein, C.S. Exponential temperature dependence of young's modulus for several oxides. *Phys. Rev.* **1961**, *122*, 1754–1759. [[CrossRef](#)]
15. Chen, J.; Nittala, K.; Forrester, J.S.; Jones, J.L.; Deng, J.; Yu, R.; Xing, X. The role of spontaneous polarization in the negative thermal expansion of tetragonal PbTiO_3 -based compounds. *J. Am. Chem. Soc.* **2011**, *133*, 11114–11117. [[CrossRef](#)]
16. Yamada, I.; Tsuchida, K.; Ohgushi, K.; Hayashi, N.; Kim, J.; Tsuji, N.; Takahashi, R.; Matsushita, M.; Nishiyama, N.; Inoue, T.; et al. Giant negative thermal expansion in the iron perovskite $\text{SrCu}_3\text{Fe}_4\text{O}_{12}$. *Angew. Chem. Int. Ed.* **2011**, *50*, 6579–6582. [[CrossRef](#)]
17. Romao, C.P.; Miller, K.J.; Whitman, C.A.; White, M.A. *Comprehensive Inorganic Chemistry II Negative Thermal Expansion (Thermomiotic) Materials*; Elsevier: Oxford, UK, 2013; Volume 4, pp. 128–151.
18. Takenaka, K.; Takagi, H. Giant negative thermal expansion in Ge-doped anti-perovskite manganese nitrides. *Appl. Phys. Lett.* **2005**, *87*, 261902. [[CrossRef](#)]
19. Walker, E. Anomalous temperature behaviour of the shear elastic constant C_{44} in vanadium. *Solid State Commun.* **1978**, *28*, 587–589. [[CrossRef](#)]
20. Armstrong, P.E.; Dickinson, J.M.; Brown, H.L. Temperature dependence of the elastic stiffness coefficients of niobium (columbium). *Trans. Am. Inst. Min. Metall. Pet. Eng.* **1966**, *236*, 1404.
21. Walker, E.; Bujard, P. Anomalous temperature behaviour of the shear elastic constant C_{44} in tantalum. *Solid State Commun.* **1980**, *34*, 691–693. [[CrossRef](#)]
22. Rayne, J.A. Elastic Constants of Palladium from 4.2-300 K. *Phys. Rev.* **1960**, *118*, 1545–1549. [[CrossRef](#)]
23. Macfarlane, R.E.; Rayne, J.A.; Jones, C.K. Anomalous temperature dependence of shear modulus C_{44} for Platinum. *Phys. Lett.* **1965**, *18*, 91–92. [[CrossRef](#)]
24. Walker, E.; Ortelli, J.; Peter, M. Elastic constants of monocrystalline alloys of Pd–Rh and Pd–Ag between 4.2 K and 300 K. *Phys. Lett. A* **1970**, *31*, 240–241. [[CrossRef](#)]
25. Ashkenazi, J.; Dacorogna, M.; Peter, M.; Talmor, Y.; Walker, E.; Steinemann, S. Elastic constants in Nb–Zr alloys from zero temperature to the melting point: Experiment and theory. *Phys. Rev. B* **1978**, *18*, 4120–4131. [[CrossRef](#)]
26. Bujard, P.; Sanjines, R.; Walker, E.; Ashkenazi, J.; Peter, M. Elastic constants in Nb–Mo alloys from zero temperature to the melting point: Experiment and theory. *J. Phys. F* **1981**, *11*, 775. [[CrossRef](#)]
27. Keuter, P.; Music, D.; Schnabel, V.; Stuer, M.; Schneider, J.M. From qualitative to quantitative description of the anomalous thermoelastic behavior of V, Nb, Ta, Pd and Pt. *J. Phys. Condens. Matter* **2019**, *31*, 225402. [[CrossRef](#)]
28. Keuter, P.; Music, D.; Stuer, M.; Schneider, J.M. Electronic structure tuning of the anomalous thermoelastic behavior in Nb–X (X = Zr, V, Mo) solid solutions. *J. Appl. Phys.* **2019**, *125*, 215103. [[CrossRef](#)]
29. Keuter, P.; Music, D.; Stuer, M.; Schneider, J.M. Temperature and impurity induced stabilization of cubic HfV_2 laves phase. *Condens. Matter* **2019**, *4*, 63. [[CrossRef](#)]
30. Huang, L.; Vitos, L.; Kwon, S.K.; Johansson, B.; Ahuja, R. Thermoelastic properties of random alloys from first-principles theory. *Phys. Rev. B* **2006**, *73*, 104203. [[CrossRef](#)]
31. Huang, L.; Ramzan, M.; Vitos, L.; Johansson, B.; Ahuja, R. Anomalous temperature dependence of elastic constant c_{44} in V, Nb, Ta, Pd, and Pt. *J. Phys. Chem. Solids* **2010**, *71*, 1065–1068. [[CrossRef](#)]

32. Lüthi, B.; Herrmann, M.; Assmus, W.; Schmidt, H.; Rietschel, H.; Wühl, H.; Gottwick, U.; Sparr, G.; Steglich, F. Normal-state and superconducting properties of HfV₂. *Z. Phys. B Condens. Matter* **1985**, *60*, 387–392. [[CrossRef](#)]
33. Rudy, E.; Windisch, S. The phase diagrams hafnium-vanadium and hafnium-chromium. *J. Less Common. Met.* **1968**, *15*, 13–27. [[CrossRef](#)]
34. Finlayson, T.R.; Lanston, E.J.; Simpson, M.A.; Gibbs, E.E.; Smith, T.F. Elastic properties of (Hf,Zr)V₂ superconducting compounds. *J. Phys. F* **1978**, *8*, 2269. [[CrossRef](#)]
35. Balankin, A.S.; Skorov, D.M. Anomalies of elastic moduli in ZrV₂ and HfV₂ Laves phases at high temperatures. *Sov. Phys. Solid State* **1982**, *24*, 681–682.
36. Pushkarev, E.A.; Petrenko, N.S.; Finkel, V.A. Thermal expansion of the superconducting compound HfV₂ at low temperatures. *Phys. Status Solidi A* **1978**, *47*, K145–K148. [[CrossRef](#)]
37. Atfield, J.P. Mechanisms and Materials for NTE. *Front. Chem.* **2018**, *6*. [[CrossRef](#)] [[PubMed](#)]
38. Mary, T.A.; Evans, J.S.O.; Vogt, T.; Sleight, A.W. Negative thermal expansion from 0.3 to 1050 Kelvin in ZrW₂O₈. *Science* **1996**, *272*, 90–92. [[CrossRef](#)]
39. Evans, J.S.O.; Mary, T.A.; Sleight, A.W. Negative thermal expansion materials. *Phys. B Condens. Matter* **1997**, *241–243*, 311–316. [[CrossRef](#)]
40. Hisashige, T.; Yamaguchi, T.; Tsuji, Y.; Yamamura, T. Phase Transition of Zr_{1-x}Hf_xV₂O₇ solid solutions having negative thermal expansion. *J. Ceram. Soc. Jpn.* **2006**, *114*, 607–611. [[CrossRef](#)]
41. Turquat, C.; Muller, C.; Nigrelli, E.; Leroux, C.; Soubeyroux, J.L.; Nihoul, G. Structural investigation of temperature-induced phase transitions in HfV₂O₇. *Eur. Phys. J. Appl. Phys.* **2000**, *10*, 15–27. [[CrossRef](#)]
42. Sutton, M.S.; Talghader, J. Micromachined negative thermal expansion thin films. *J. Microelectromechanical Syst.* **2004**, *13*, 1148–1151. [[CrossRef](#)]
43. Liu, H.; Yang, L.; Zhang, Z.; Pan, K.; Zhang, F.; Cheng, H.; Zeng, X.; Chen, X. Preparation and optical, nanomechanical, negative thermal expansion properties of Sc₂W₃O₁₂ thin film grown by pulsed laser deposition. *Ceram. Int.* **2016**, *42*, 8809–8814. [[CrossRef](#)]
44. Liu, H.; Zhang, Z.; Zhang, W.; Chen, X.; Cheng, X. Negative thermal expansion ZrW₂O₈ thin films prepared by pulsed laser deposition. *Surf. Coat. Technol.* **2011**, *205*, 5073–5076. [[CrossRef](#)]
45. Liu, H.; Pan, K.; Jin, Q.; Zhang, Z.; Wang, G.; Zeng, X. Negative thermal expansion and shift in phase transition temperature in Mo-substituted ZrW₂O₈ thin films prepared by pulsed laser deposition. *Ceram. Int.* **2014**, *40*, 3873–3878. [[CrossRef](#)]
46. Bepalov, I.; Datler, M.; Buhr, S.; Drachsel, W.; Ruppachter, G.; Suchorski, Y. Initial stages of oxide formation on the Zr surface at low oxygen pressure: An in situ FIM and XPS study. *Ultramicroscopy* **2015**, *159*, 147–151. [[CrossRef](#)]
47. Laguna, O.H.; Pérez, A.; Centeno, M.A.; Odriozola, J.A. Synergy between gold and oxygen vacancies in gold supported on Zr-doped ceria catalysts for the CO oxidation. *Appl. Catal. B* **2015**, *176–177*, 385–395. [[CrossRef](#)]
48. Schneider, J.M.; Hjörvarsson, B.; Wang, X.; Hultman, L. On the effect of hydrogen incorporation in strontium titanate layers grown by high vacuum magnetron sputtering. *Appl. Phys. Lett.* **1999**, *75*, 3476–3478. [[CrossRef](#)]
49. Ravensburg, A.L.; Keuter, P.; Music, D.; Miljanovic, D.J.; Schneider, J.M. Experimental and Theoretical Investigation of the Elastic Properties of HfV₂O₇. *Crystals* **2020**, *10*, 172. [[CrossRef](#)]
50. Zhang, Y.; Whitlow, H.J.; Winzell, T.; Bubb, I.F.; Sajavaara, T.; Arstila, K.; Keinonen, J. Detection efficiency of time-of-flight energy elastic recoil detection analysis systems. *Nucl. Instrum. Methods Phys. Res. B* **1999**, *149*, 477–489. [[CrossRef](#)]
51. Janson, M.S. *Contes Instruction Manual*; Uppsala University: Uppsala, Sweden, 2004.
52. Bragg, W.H.; Bragg, W.L. The reflection of X-rays by crystals. *Proc R. Soc. Lond. Ser. A Contain. Pap. Math. Phys. Character* **1913**, *88*, 428–438. [[CrossRef](#)]
53. Langford, R.M.; Rogers, M. In situ lift-out: Steps to improve yield and a comparison with other FIB TEM sample preparation techniques. *Micron* **2008**, *39*, 1325–1330. [[CrossRef](#)]
54. Hohenberg, P.; Kohn, W. Inhomogeneous electron gas. *Phys. Rev.* **1964**, *136*, B864–B871. [[CrossRef](#)]
55. Kresse, G.; Hafner, J. Ab initio molecular dynamics for open-shell transition metals. *Phys. Rev. B* **1993**, *48*, 13115–13118. [[CrossRef](#)] [[PubMed](#)]

56. Kresse, G.; Hafner, J. Ab initio molecular-dynamics simulation of the liquid-metal-amorphous-semiconductor transition in germanium. *Phys. Rev. B* **1994**, *49*, 14251–14269. [[CrossRef](#)] [[PubMed](#)]
57. Perdew, J.P.; Burke, K.; Ernzerhof, M. Generalized gradient approximation made simple. *Phys. Rev. Lett.* **1996**, *77*, 3865–3868. [[CrossRef](#)]
58. Monkhorst, H.J.; Pack, J.D. Special points for Brillouin-zone integrations. *Phys. Rev. B* **1976**, *13*, 5188–5192. [[CrossRef](#)]
59. Birch, F. Finite Elastic Strain of Cubic Crystals. *Phys. Rev.* **1947**, *71*, 809–824. [[CrossRef](#)]
60. Murnaghan, F.D. The compressibility of media under extreme pressures. *Proc. Natl. Acad. Sci. USA* **1944**, *15*, 244–247. [[CrossRef](#)]
61. Drymiotis, F.R.; Ledbetter, H.; Betts, J.B.; Kimura, T.; Lashley, J.C.; Migliori, A.; Ramirez, A.P.; Kowach, G.R.; Van Duijn, J. Monocrystal elastic constants of the negative-thermal-expansion compound zirconium tungstate (ZrW_2O_8). *Phys. Rev. Lett.* **2004**, *93*, 025502. [[CrossRef](#)]
62. De Buysser, K.; Lommens, P.; De Meyer, C.; Bruneel, E.; Hoste, S.; Van Driessche, I. ZrO_2 - ZrW_2O_8 composites with tailor-made thermal expansion. *Ceram. Silik.* **2004**, *48*, 139–144.
63. Evans, J.S.O.; Mary, T.A.; Vogt, T.; Subramanian, M.A.; Sleight, A.W. Negative thermal expansion in ZrW_2O_8 and HfW_2O_8 . *Chem. Mater.* **1996**, *8*, 2809–2823. [[CrossRef](#)]
64. Yamamura, Y.; Horikoshi, A.; Yasuzuka, S.; Saitoh, H.; Saito, K. Negative thermal expansion emerging upon structural phase transition in ZrV_2O_7 and HfV_2O_7 . *Dalt. Trans.* **2011**, *40*, 2242–2248. [[CrossRef](#)] [[PubMed](#)]
65. Romao, C.P.; Marinkovic, B.A.; Werner-Zwanziger, U.; White, M.A. Thermal expansion reduction in alumina-toughened zirconia by incorporation of zirconium tungstate and aluminum tungstate. *J. Am. Ceram. Soc.* **2015**, *98*, 2858–2865. [[CrossRef](#)]
66. Kingery, W.D.; Bowen, H.K.; Uhlmann, D.R. *Introduction to Ceramics*; Wiley: New York, NY, USA, 1960.
67. Chen, H.-Y.; Lu, F.-H. Oxidation behavior of titanium nitride films. *J. Vac. Sci. Technol. A* **2005**, *23*. [[CrossRef](#)]
68. Stelzer, B.; Momma, M.; Schneider, J.M. Autonomously Self-Reporting Hard Coatings: Tracking the temporal oxidation behavior of tin by in situ sheet resistance measurements. *Adv. Funct. Mater.* **2020**, *30*, 2000146. [[CrossRef](#)]
69. Eickert, S.; Hecht, H.; von Minnigerode, G. Formation area of amorphous thin V–Zr films prepared by cocondensation on hot substrates. *Z. Phys. B Condens. Matter* **1992**, *88*, 35–38. [[CrossRef](#)]
70. Shi, L.Q.; Xu, S.L. Phase transformations of sputtered ZrV_2 films after annealing and hydrogenation. *J. Vac. Sci. Technol. A* **2006**, *24*, 190–194. [[CrossRef](#)]
71. King, D.J.M.; Middleburgh, S.C.; Liu, A.C.Y.; Tahini, H.A.; Lumpkin, G.R.; Cortie, M.B. Formation and structure of V–Zr amorphous alloy thin films. *Acta Mater.* **2015**, *83*, 269–275. [[CrossRef](#)]
72. Chihi, T.; Fatmi, M.; Ghebouli, B. Ab initio calculations for properties of laves phase V_2M ($\text{M} = \text{Zr}, \text{Hf}, \text{Ta}$) compounds. *Am. J. Mod. Phys.* **2013**, *2*, 88–92. [[CrossRef](#)]
73. Lumley, S.C.; Murphy, S.T.; Burr, P.A.; Grimes, R.W.; Chard-Tuckey, P.R.; Wenman, M.R. The stability of alloying additions in Zirconium. *J. Nucl. Mater.* **2013**, *437*, 122–129. [[CrossRef](#)]
74. Levy, O.; Hart, G.L.W.; Curtarolo, S. Hafnium binary alloys from experiments and first principles. *Acta Mater.* **2010**, *58*, 2887–2897. [[CrossRef](#)]
75. Vřešťál, J.; Pavlů, J.; Wdowik, U.D.; Šob, M. Modelling of phase equilibria in the Hf–V system below room temperature. *J. Min. Metall. Sect. B Metall.* **2017**, *53*, 239–247. [[CrossRef](#)]
76. Parsons, M.J.; Brown, P.J.; Crangle, J.; Neumann, K.U.; Ouladdiaf, B.; Smith, T.J.; Zayer, N.K.; Ziebeck, K.R.A. A study of the structural phase transformation and superconductivity in HfV_2 . *J. Phys. Condens. Matter* **1998**, *10*, 8523. [[CrossRef](#)]
77. Zhao, Y.; Chu, F.; Von Dreele, R.B.; Zhu, Q. Structural phase transitions of HfV_2 at low temperatures. *Acta Crystallogr. Sect. B Struct. Sci.* **2000**, *56*, 601–606. [[CrossRef](#)]
78. Rapp, Ö.; Benediktsson, G. Latent heat of structural transformations in ZrV_2 and HfV_2 . *Phys. Lett. A* **1979**, *74*, 449–452. [[CrossRef](#)]
79. Kim, W.-Y.; Luzzi, D.E.; Pope, D.P. Room temperature deformation behavior of the Hf–V–Ta C15 Laves phase. *Intermetallics* **2003**, *11*, 257–267. [[CrossRef](#)]
80. Bolvardi, H.; Emmerlich, J.; Mráz, S.; Arndt, M.; Rudigier, H.; Schneider, J.M. Low temperature synthesis of Mo_2BC thin films. *Thin Solid Films* **2013**, *542*, 5–7. [[CrossRef](#)]
81. Smith, T.F.; Shelton, R.N.; Lawson, A.C. Superconductivity and structural instability of $(\text{Hf}, \text{Zr})\text{V}_2$ and $(\text{Hf}, \text{Ta})\text{V}_2$ alloys at high pressure. *J. Phys. F* **1973**, *3*, 2157. [[CrossRef](#)]

82. Forker, M.; Herz, W.; Simon, D. Impurity trapping in the laves phase HfV₂ detected by perturbed angular correlations. *J. Phys. Condens. Matter* **1992**, *4*, 213. [[CrossRef](#)]
83. Greczynski, G.; Petrov, I.; Greene, J.E.; Hultman, L. Al capping layers for nondestructive x-ray photoelectron spectroscopy analyses of transition-metal nitride thin films. *J. Vac. Sci. Technol. A* **2015**, *33*, 05E101. [[CrossRef](#)]
84. Cramer, S.D.; Covino, B.S. *ASM Metals Handbook—Corrosion: Fundamentals, Testing, and Protection*; ASM International: Materials Park Campus, OH, USA, 2003; Volume 13A.
85. Kang, Y.-B. Critical evaluation and thermodynamic optimization of the VO–VO_{2.5} system. *J. Eur. Ceram. Soc.* **2012**, *32*, 3187–3198. [[CrossRef](#)]
86. Wang, J.; Li, H.P.; Stevens, R. Hafnia and hafnia-toughened ceramics. *J. Mater. Sci.* **1992**, *27*, 5397–5430. [[CrossRef](#)]
87. Turquat, C.; Leroux, C.; Gloter, A.; Serin, V.; Nihoul, G. V-doped HfO₂: Thermal stability and vanadium valence. *Int. J. Inorg. Mater.* **2001**, *3*, 1025–1032. [[CrossRef](#)]
88. Turquat, C.; Leroux, C.; Roubin, M.; Nihoul, G. Vanadium-doped hafnia: Elaboration and structural characterization. *Solid State Sci.* **1999**, *1*, 3–13. [[CrossRef](#)]
89. Manory, R.; Mori, T.; Shimizu, I.; Miyake, S.; Kimmel, G. Growth and structure control of HfO_{2-x} films with cubic and tetragonal structures obtained by ion beam assisted deposition. *J. Vac. Sci. Technol. A* **2002**, *20*. [[CrossRef](#)]
90. Hemamala, U.L.C.; El-Ghoussein, F.; Goedken, A.M.; Chen, B.; Leroux, C.; Kruger, M.B. High-pressure x-ray diffraction and Raman spectroscopy of HfV₂O₇. *Phys. Rev. B* **2004**, *70*, 70. [[CrossRef](#)]
91. Pryde, A.K.A.; Hammonds, K.D.; Dove, M.T.; Heine, V.; Gale, J.D.; Warren, M.C. Origin of the negative thermal expansion in ZrW₂O₈ and ZrV₂O₇. *J. Phys. Condens. Matter* **1996**, *8*, 10973–10982. [[CrossRef](#)]
92. Mittal, R.; Chaplot, S.L. Lattice dynamica calculation of negative thermal expansion in ZrV₂O₇ and HfV₂O₇. *Phys. Rev. B* **2008**, *78*. [[CrossRef](#)]
93. Korthuis, V.; Khosrovani, N.; Sleight, A.W.; Roberts, N.; Dupree, R.; Warren, W.W., Jr. Negative Thermal expansion and phase transitions in the ZrV_{2-x}P_xO₇ series. *Chem. Mater.* **1995**, *7*, 412–417. [[CrossRef](#)]
94. Evans, J.S.O.; Hanson, J.C.; Sleight, A.W. Room-temperature superstructure of ZrV₂O₇. *Acta Crystallogr. Sect. B* **1998**, *54*, 705–713. [[CrossRef](#)]
95. Khosrovani, N.; Sleight, A.W.; Vogt, T. Structure of ZrV₂O₇ from –263 to 470 °C. *J. Solid State Chem.* **1997**, *132*, 355–360. [[CrossRef](#)]
96. Withers, R.L.; Evans, J.S.O.; Hanson, J.; Sleight, A.W. An in situ temperature-dependent electron and X-ray diffraction study of structural phase transitions in ZrV₂O₇. *J. Solid State Chem.* **1998**, *137*, 161–167. [[CrossRef](#)]
97. Baran, E.J. The unit cell of hafnium divanadate. *J. Less Common. Met.* **1976**, *46*, 343–345. [[CrossRef](#)]

Publisher’s Note: MDPI stays neutral with regard to jurisdictional claims in published maps and institutional affiliations.



© 2020 by the authors. Licensee MDPI, Basel, Switzerland. This article is an open access article distributed under the terms and conditions of the Creative Commons Attribution (CC BY) license (<http://creativecommons.org/licenses/by/4.0/>).